# Ionospheric and thermospheric variations associated with prompt penetration electric fields

G. Lu,[1] L. Goncharenko,[2] M. J. Nicolls,[3] A. Maute,[1] A. Coster,[2] and L. J. Paxton[4]

Received 27 March 2012; revised 19 May 2012; accepted 25 June 2012; published 10 August 2012.

[1] This paper presents a comprehensive modeling investigation of ionospheric and thermospheric variations during a prompt penetration electric field (PPEF) event that took place on 9 November 2004, using the Thermosphere-Ionosphere-Mesosphere Electrodynamic General Circulation Model (TIMEGCM). The simulation results reveal complex latitudinal and longitudinal/local-time variations in vertical ion drift in the middle- and low-latitude regions owing to the competing influences of electric fields and neutral winds. It is found that electric fields are the dominant driver of vertical ion drift at the magnetic equator; at midlatitudes, however, vertical ion drift driven by disturbance meridional winds exceeds that driven by electric fields. The temporal evolution of the UT-latitude electron density profile from the simulation depicts clearly a super-fountain effect caused by the PPEF, including the initial slow-rise of the equatorial F-layer peak height, the split of the F-layer peak density, and the subsequent downward diffusion of the density peaks along magnetic field lines. Correspondingly, low-latitude total electron content (TEC) becomes bifurcated around the magnetic equator. The $O/N_2$ column density ratio, on the other hand, shows very little variations during this PPEF event, excluding composition change as a potential mechanism for the TEC variations. By using realistic, time-dependent, high-latitude electric potential and auroral precipitation patterns to drive the TIMEGCM, the model is able to successfully reproduce the large vertical ion drift of $\sim$120 m/s over the Jicamarca incoherent radar (IS) in Peru, which is the largest daytime ion drift ever recorded by the radar. The simulation results are validated with several key observations from IS radars, ground GPS-TEC network, and the TIMED-GUVI $O/N_2$ column density ratio. The model-data intercomparison also reveals some deficiencies in the TIMEGCM, particularly the limitations imposed by its upper boundary height as well as the prescribed $O^+$ flux.

**Citation:** Lu, G., L. Goncharenko, M. J. Nicolls, A. Maute, A. Coster, and L. J. Paxton (2012), Ionospheric and thermospheric variations associated with prompt penetration electric fields, *J. Geophys. Res.*, *117*, A08312, doi:10.1029/2012JA017769.

## 1. Introduction

[2] The middle- and low-latitude ionosphere and thermosphere are affected by a number of externally and internally driven dynamical and electrodynamical processes. At the magnetic equator, an eastward electric field causes heavy ions to drift upward across magnetic field lines to an altitude where the upward $\boldsymbol{E} \times \boldsymbol{B}$ motion is toppled by pressure gradient and gravity so that ions begin to diffuse downward along magnetic field lines to higher latitudes. This process is referred to as the fountain effect, which is mainly responsible for the formation of the equatorial ionization anomaly [e.g., *Hanson and Moffet*, 1966; *King*, 1968; *Anderson*, 1973]. Under quiet geomagnetic conditions the fountain effect is most pronounced near dusk where there exists a large eastward electric field in association with the "pre-reversal" enhancement [*Woodman*, 1970]. During active time, electric fields associated with a strongly southward IMF point from dawn to dusk across the polar cap. A fraction of the dawn-to-dusk electric fields can penetrate spontaneously to mid-latitudes and low latitudes via current leakage through the conducting ionosphere, yielding an eastward electric field on the dayside and a westward electric field on the nightside [*Fejer and Scherliess*, 1995, 1997]. Since the penetration electric fields are much larger than the typical quiet time electric fields generated by thermospheric winds that are modulated by atmospheric tides, the middle- and low-latitude ionosphere is strongly influenced by the penetration electric

[1]High Altitude Observatory, National Center for Atmospheric Research, Boulder, Colorado, USA.
[2]Haystack Observatory, Massachusetts Institute of Technology, Westford, Massachusetts, USA.
[3]Center for Geospace Studies, SRI International, Menlo Park, California, USA.
[4]Applied Physics Laboratory, Johns Hopkins University, Laurel, Maryland, USA.

Corresponding author: G. Lu, High Altitude Observatory, National Center for Atmospheric Research, Boulder, CO 80301, USA. (ganglu@ucar.edu)


0148-0227/12/2012JA017769

fields. The eastward (westward) penetration electric fields force plasmas to move upward (downward), which in turn excites (inhibits) ionospheric irregularities such as equatorial spread *F* [*Fejer et al.*, 1999].

[3] In addition to the penetration of high-latitude electric field, enhanced storm-time Joule heating dissipation in the auroral zones produces large horizontal pressure gradients that drive neutral winds equatorward toward middle and low latitudes, even into the opposite hemisphere. The neutral wind surges also have a strong longitudinal dependence, and thus produce longitudinal structures in the mid- and low-latitude ionosphere. Because of the complex interplay among the different drivers, it is often difficult to distinguish one driving force from another based on observations alone.

[4] Though the prompt penetration electric field (PPEF) effects on the ionosphere and thermosphere have been investigated for nearly four decades, there is a renewed interest on the topic in recent years due to significant impacts that the PPEF may have on space weather by producing ionospheric density gradients and disrupting communication/navigation systems [*Kelley and Retterer*, 2008; *Basu et al.*, 2001]. The event on 9 November 2004 showcases some distinctive ionospheric/thermospheric disturbances caused by the PPEF, and has drawn considerable attention in the research community [e.g., *Grigorenko et al.*, 2007; *Fejer et al.*, 2007; *Sahai et al.*, 2009a, 2009b; *Mannucci et al.*, 2009; *Kelley et al.*, 2010; *Erickson et al.* 2010]. These studies have largely focused on the observational aspect of the event based a particular set of data. So far only limited numerical studies of the event have been carried out [e.g., *Retterer and Kelley*, 2010; *Retterer et al.*, 2010; *Hei and Valladares*, 2010], and they are based on 2D models that require prescribed neutral density, temperature, winds, and plasma drifts as input. In this paper we present a comprehensive modeling investigation of the event using the Thermosphere-Ionosphere-Mesosphere-Electrodynamic General Circulation Model (TIMEGCM) developed at the National Center for Atmospheric Research (NCAR), which is a 3D global model with fully self-consistent calculations of ion-neutral properties. We demonstrate that, by incorporating realistic, time-dependent, high-latitude electric field and auroral energy dissipation, the TIMEGCM is able to reproduce several key features shown in various observations. The main purpose of the study is to elucidate the underlying physical processes responsible for the ionospheric and thermospheric disturbances associated with the PPEF in light of numerical simulations as well as data-model intercomparison.

## 2. Model Results

### 2.1. Model Description

[5] The TIMEGCM [*Roble and Ridley*, 1994] is a first-principle upper atmospheric general circulation model that solves the Eulerian continuity, momentum, and energy equations for the coupled thermosphere-ionosphere system. It utilizes a spherical coordinate system fixed with respect to the rotating Earth, with latitude and longitude as the horizontal axes and pressure surfaces as the vertical axis. The model has 49 constant-pressure levels vertically extending from ~35 km up to ~700 km, and has horizontal resolution of 5° × 5° in latitude and longitude. The external forcing of the TIMEGCM are solar spectral irradiance in EUV and UV range, magnetospheric energy input in the form of auroral energetic particle precipitation and ionospheric plasma convection driven by the solar wind-magnetosphere interaction, and the amplitudes and phases of tides from the lower atmosphere. In this study, the model is forced at the lower boundary by migrating diurnal and semi-diurnal tides derived from the Global-Scale Wave Model (GSWM) [*Hagan and Forbes*, 2002, 2003], together with daily averaged observations from the National Center for Environment Predictions (NCEP) analysis to represent other longer wavelength atmospheric forcing.

[6] At its upper boundary, the TIMEGCM is driven by the time-dependent high-latitude ionospheric electric potential and auroral precipitation patterns derived from the Assimilative Mapping of Ionospheric Electrodynamics (AMIE) procedure [*Richmond and Kamide*, 1988]. The objective of the AMIE procedure is to obtain optimal estimates of high-latitude ionospheric electrodynamic fields by combining various direct and indirect observations of these fields. The data inputs to AMIE for this event include magnetic field perturbations measured at 189 ground magnetometer stations, auroral particle measurements from 3 Defense Meteorological Satellite Program (DMSP) satellites, 3 NOAA satellites, auroral images from the Global Ultraviolet Imager (GUVI) onboard the Thermosphere Ionosphere Mesosphere Energetics and Dynamics (TIMED) satellite, and ion drift measurements from the DMSP spacecraft and the Super-DARN radar network. More detailed information on the AMIE results for this particular event can be found in *Lu et al.* [2011]. The AMIE patterns in the northern and southern hemispheres have a 5-min cadence, and are interpolated in time to drive the TIMEGCM that runs at a time step of 1 min.

[7] Solar EUV and UV fluxes used in the model are based on the daily F10.7 index, which was $138.1 \times 10^{-22}$ W m$^{-2}$ Hz$^{-1}$on 9 November 2004. Another upper boundary input is the $O^+$ flux, which is set to a default value of $2 \times 10^8$ cm$^{-3}$ s$^{-1}$. The $O^+$ flux is upward during the day and downward at night, and is interpolated between the daytime and nighttime values as a function of solar zenith angle. The $O^+$ flux also varies with magnetic latitude, but its magnitude and morphology remained unchanged throughout the simulation. The default O+ flux value is based on previous numerical experiments against empirical models such as the International Reference Ionosphere (IRI) in terms of global means under quiet conditions [*Fesen et al.*, 2000]. This specification of the $O^+$ flux is clearly an oversimplification of plasmaspheric conditions that are known to change drastically during geomagnetic storms [e.g., *Gallagher et al.*, 2000; *Pierrard and Stegen*, 2008]. As discussed in *Lu et al.* [2001], the $O^+$ flux imposed at the model's upper boundary has a significant influence on the *F* region electron density and peak height.

### 2.2. Geophysical Conditions

[8] Figure 1a shows the interplanetary electric field (IEF) between 12:00 UT on 9 November 2004 and 08:00 UT on 10 November 2004. Here the IEF (more precisely, the east-west component of the IEF) is defined as the product of the solar bulk speed $V$ and the IMF $B_z$ component as measured by the ACE spacecraft located at (242, 22, −15) $R_E$ in GSE

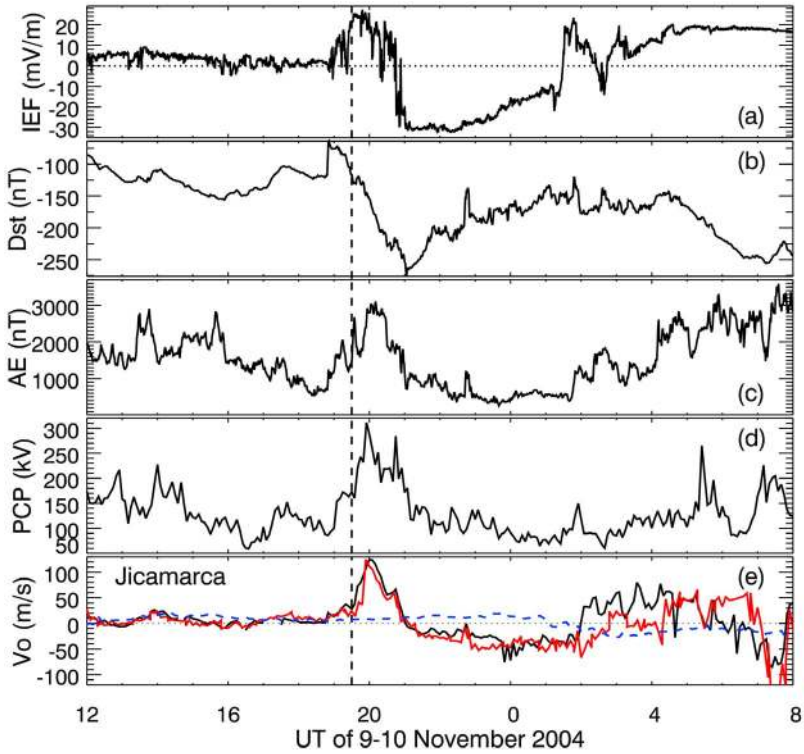


**Figure 1.** Distributions of (a) the interplanetary electric field (IEF), (b) the Dst index, (c) the AE index, (d) the polar-cap potential (PCP) drop derived from AMIE, and (e) vertical ion drift over Jicamarca. The black line is from the Jicamarca radar measurements, the blue dashed line represents the quiet time vertical ion drift measured by the radar, and the red line is the modeled vertical ion drift from the TIMEGCM. The vertical dashed line at 19:30 UT denotes the time when vertical ion drift increased rapidly over Jicamarca.

coordinates. A time shift of 28 min has been applied to the ACE data plotted in Figure 1a to account for the solar wind propagation from its upstream location to the Earth, and the determination of this time shift is described in *Lu et al.* [2011]. Positive IEF values correspond to southward $B_z$ and negative IEF values for northward $B_z$. As noted by *Lu et al.* [2011], the positive IEF period was mainly associated with the sheath region where the solar wind and IMF were compressed from behind by a fast-moving interplanetary corona mass ejection (ICME). The IEF increased to ~25 mV/m between 19:30 and 20:00 UT. It decreased subsequently and became negative around 21:00 UT when $B_z$ turned northward abruptly and remained negative until 01:20 UT on 10 November. Figures 1b and 1c display the *Dst* and *AE* indices. The *Dst* index is derived from the measurements of 52 ground magnetometers located below |40°| magnetic latitude (MLAT), and the *AE* index is derived from the north-south component of magnetic perturbations at 80 magnetometer stations located between |55°| and |76°| MLAT in the northern and southern hemispheres. Both indices have a temporal resolution of 1 min. As discussed in *Lu et al.* [2011], a storm sudden commencement as manifested by the rapid increase in *Dst* at 18:49 UT was prompted by the arrival of an interplanetary shock impinged on the dayside of the magnetopause. During the interval of positive IEF, the *Dst* index dropped to near −280 nT, making it a major storm [*Gonzalez et al.*, 1994]. The storm started to recover after the IEF ($B_z$) became negative (positive). During the same period *AE* had increased to ~3000 nT around 20:00 UT, an indication of strong auroral electric current at high latitudes. Figure 1d shows the polar-cap potential (PCP) drop derived from AMIE, which reached a peak value of ~300 kV at 20:00 UT. Both the *AE* index and the polar-cap potential drop decreased during the period of negative IEF, and then increased again when the IEF became positive after 01:00 UT on 10 November 2004 except a brief negative excursion around 02:40 UT.

[9] As noted by *Kelley et al.* [2010], the maximum IEF value of ~25 mV/m on 9 November is ranked only the 10th out of a total of 11 superstorms in solar cycle 23. Yet, the event serves as a primary example of prompt penetration electric fields. Figure 1e depicts the vertical ion drift over Jicamarca at 11.9°S and 76.8°W, which is about 1° north of the local magnetic equator. The black line shows vertical ion drift measured by the Jicamarca incoherent scatter (IS) radar. Large ion drift with a magnitude of ~120 m/s was observed around 20:00 UT on 9 November 2004. This is the largest daytime vertical ion drift ever measured by the Jicamarca radar [*Fejer et al.*, 2007; *Kelley et al.*, 2010]. For reference, the quiet time vertical ion drift is shown as the blue dashed line. The vertical dashed line at 19:30 UT denotes the time when vertical ion drift rose rapidly over Jicamarca. We denote this as the beginning of the PPEF, although the IMF actually turned southward at 18:49 UT. The red line is the modeled vertical ion drift over Jicamarca derived from the coupled AMIE-TIMEGCM simulations. Good agreement between the measured and modeled ion drift is seen on 9 November. More specifically, the rapid rise and the peak

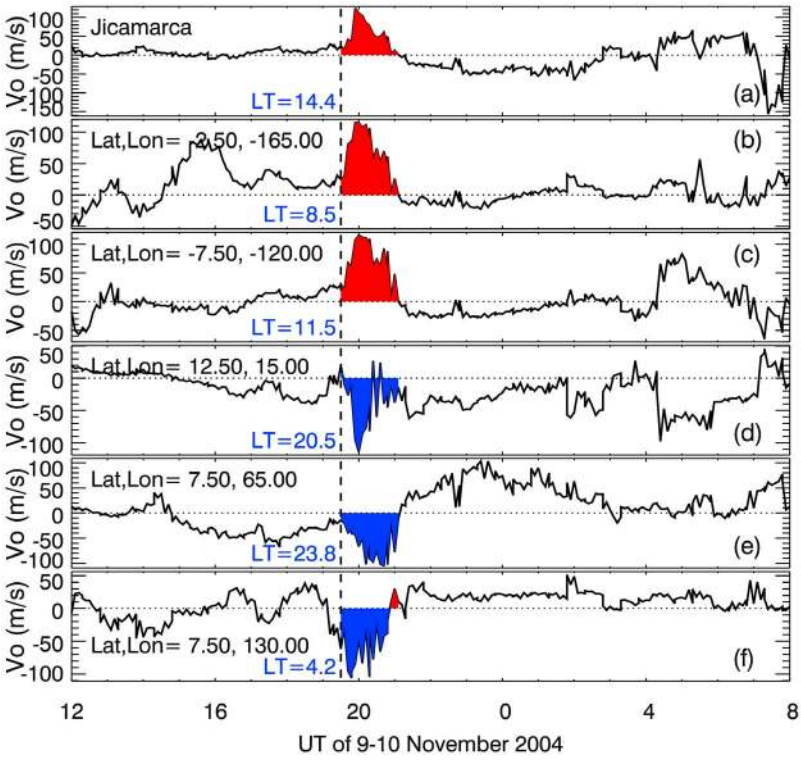


**Figure 2.** Distributions of the modeled vertical ion drift near the magnetic equator at selected longitudes. Upward drifts are highlighted in red, and downward drifts are in blue. The vertical dashed line corresponds to 1930 UT, along with the corresponding local time (LT) value at each given longitude sector.

value of vertical ion drift are both very well reproduced by the model. Note that around 00 UT when the vertical ion drift at Jicamarca is typically upward as indicated by the quiet time ion drift (the blue dashed line) due to the pre-reversal enhancement [*Fejer et al.*, 1999]. In this case, however, the vertical drift becomes downward both in radar measurements and in simulations. This reversed pre-reversal feature was noticed by *Retterer and Kelley* [2010] as well in their empirical ion drift model for the event. Though the modeled vertical ion drift still displays similar variations as observed by the radar, the agreement between the data and model has deteriorated on 10 November when a series of auroral events took place as indicated by *AE* variations shown in Figure 1c. The primary focus of this paper is thus on 9 November, particularly the period of 19:30–21:30 UT when the PPEF effects are most pronounced.

### 2.3. Vertical Ion Drift Variations

[10] Previous studies have shown that the PPEF tends to be eastward on the dayside and westward on the nightside, changing polarity near dusk [*Fejer et al.*, 1990]. With limited satellite and radar observations available for a given event, it is often difficult to assess the PPEF effects at the different latitudinal and longitudinal/local-time sectors simultaneously. In this section we present numerical simulations of thermospheric and ionospheric response to the PPEF on a global scale.

[11] Figure 2 shows the model predictions of vertical ion drift at various longitude locations near the magnetic equator, which are consistent with the local-time behavior expected from the impact of a PPEF. The top three panels show large upward drift at three dayside locations ranging from 08:30 local time (LT) to 14:24 LT at 19:30 UT when strong electric field penetration occurred. The bottom three panels, on the other hand, show downward equatorial ion drift on the nightside from 20:30 LT to 04:24 LT.

[12] Latitudinal variations associated with the PPEF are illustrated in Figure 3. Despite their close proximity in longitude, vertical ion drift over the four IS radar locations are rather different: strong upward drift over Jicamarca (11.9°S, 76.8°W), downward drift over Arecibo (18.3°N, 66.7°W) and Sondrestrom (67.0°N, 51.0°W), and downward followed by upward drift over Millstone Hill (42.6°N, 71.5°W). There seems a lack of coherency in latitudinal variations in response to the PPEF.

[13] The latitudinal and longitudinal/local-time variations are further examined in Figure 4, which displays maps of total ion drifts at 350 km altitude from 19:00 UT to 21:30 UT. Horizontal ion drifts are shown in vectors, and vertical ion drifts are shown in color with positive values for upward drifts and negative values for downward drifts. At 19:00 UT, prior to the PPEF, ion drifts are weakly upward and westward on the dayside and downward and eastward on the nightside, with a drift speed of a few 10s m/s. At 19:30 UT, the beginning of the PPEF, the dayside upward drift remains nearly the same in magnitude but has extended to the evening side. At the same time, the morning-side downward ion drift has extended to around 05 LT. At 20:00 UT, the peak of the PPEF, both the dayside upward drift and the nightside downward drift have intensified significantly, with a peak speed exceeding 100 m/s. At 20:30 and 21:00 UT, the general morphology of ion drift at mid and low latitudes is

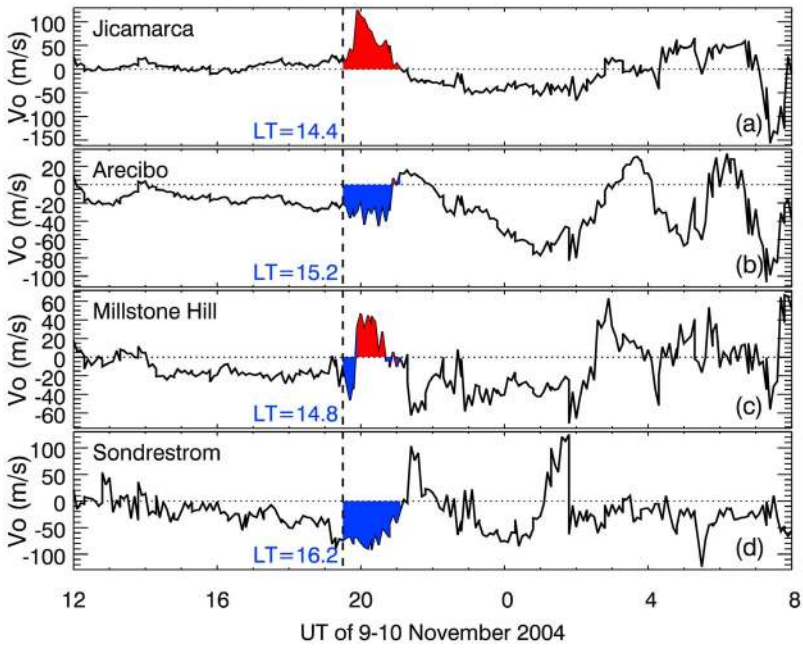


**Figure 3.** Distributions of the modeled vertical ion drift at selected latitudes corresponding to the North America IS radar chain.

about the same but the drift speed gradually reduces. At 21:30 UT, however, a significant change in morphology takes place, showing upward drift in the region from 00:00 to ~07:00 LT and downward drift in all other LT sectors near the magnetic equator. This change coincides with the change of the IMF $B_z$ component from southward to northward.

[14] Though vertical ion drift is generally upward on the dayside and downward on the nightside during the PPEF, other small-scale variations in longitude/local-time are easily noticeable. From 20:00 UT to 21:00 UT, the dayside upward drift has two peaks around 0800 and 1300 LT, respectively. While the largest downward drift is in the evening sector at 20:00 UT, it has shifted to the early morning sector at 20:30 UT and 21:00 UT, respectively. Besides the longitudinal/local-time variations, there are also significant latitudinal changes in each UT map, particularly at middle and higher latitudes and across all longitudes or local times. It is worth

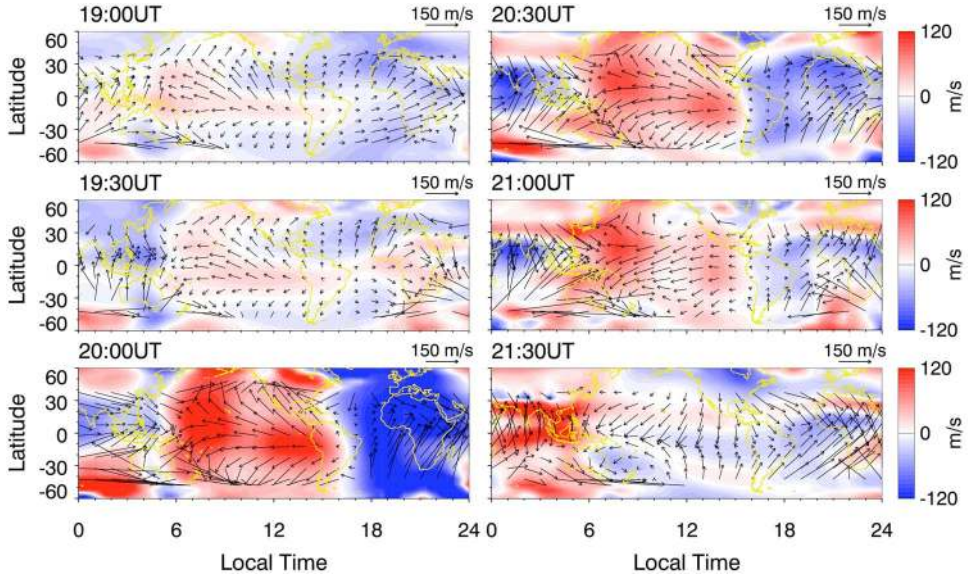


**Figure 4.** Maps of the modeled total ion drifts at 350 km from 19:00 UT to 21:30 UT. Vertical ion drifts are shown in color, and horizontal drifts are plotted as vectors. For legibility, horizontal ion drifts are plotted every 10° in latitudes and every 15° in longitude (or 1 h in local time), and large horizontal ion drifts above |45°| are not plotted.

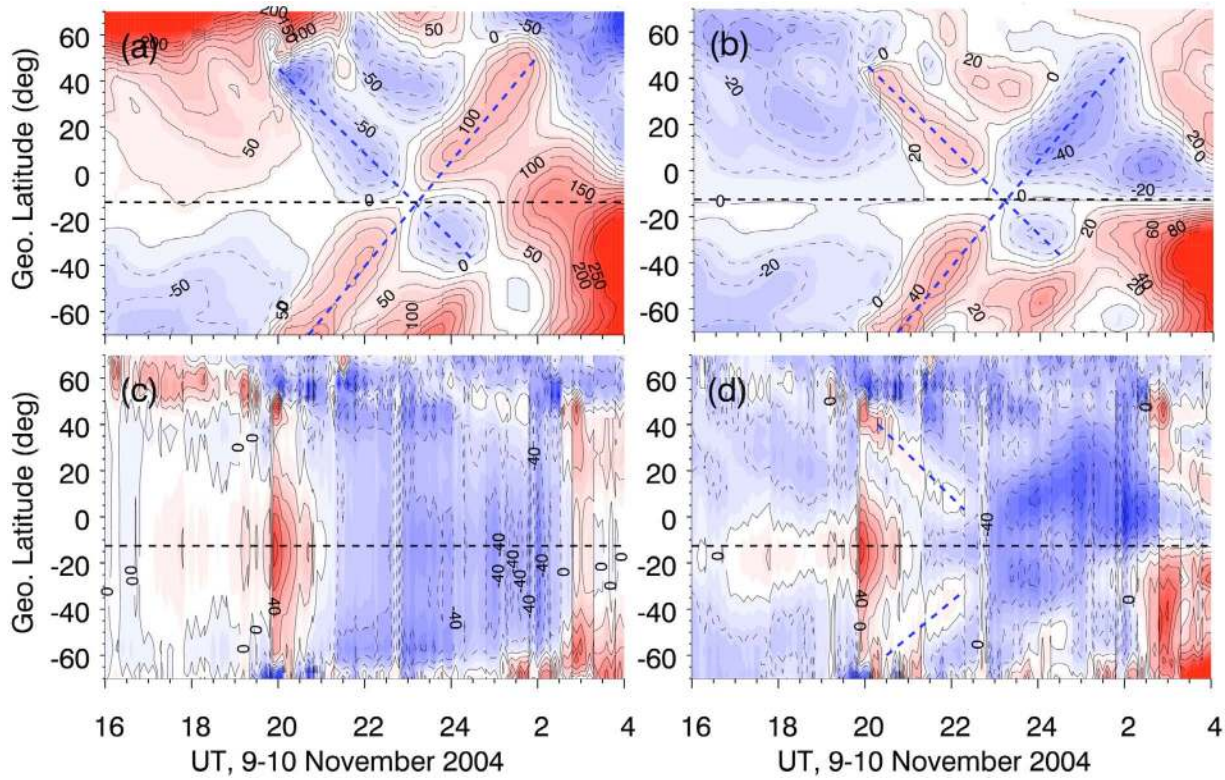


**Figure 5.** UT-Latitude distributions of (a) meridional wind, (b) vertical ion drift component due to neutral wind, (c) vertical ion drift component due to electric field, and (d) total vertical ion drift. All fields are plotted at the fixed altitude of 350 km along 75°W. The horizontal dashed line indicates local magnetic equator, and the slanted dashed lines highlight the phase propagation of the TADs.

pointing out another large-scale feature shown in horizontal ion drift, that is, the gradual change of horizontal drift direction from poleward to equatorward during the interval of 19:00–21:30 UT. As discussed below, this course of change in horizontal drift is associated with the traveling ionospheric/atmospheric disturbances rather than the PPEF itself.

[15] The complex latitudinal variations shown in Figure 3 during the interval between 19:30 and 21:00 UT are due in part to the fact that the IS radar chain happens to be located at the local time boundary between the upward vertical drifts caused by eastward dayside penetration electric fields and the downward vertical drifts associated with westward nightside penetration electric fields. However, the complex interplay between the PPEF and the disturbance neutral winds incited by strong Joule heating at high latitudes appears to be the most important factor in creating the lack of coherency in the latitudinal variations in vertical ion drift. Figure 5 shows the UT-latitude distributions of meridional wind and vertical ion drift at 350 km along 75°W. Prior to 2000 UT, the meridional wind shown in Figure 5a is poleward in both hemispheres. But the magnitude of the poleward wind is somewhat stronger in the northern hemisphere than in the southern hemisphere, consistent with a nominal summer-to-winter background circulation. Around 2000 UT, the meridional wind reverses to equatorward, showing a clear signature of the traveling atmospheric disturbances (TADs) as highlighted by the slanted blue dashed lines. The TADs originate in both the northern and southern auroral regions. They pass across each other near the local magnetic equator as indicated by the horizontal dashed line, and then penetrate into the opposite hemisphere. The phase speed is about 610 m/s for the southward propagating TAD from the northern hemisphere and about 730 m/s for the northward propagating TAD from the southern hemisphere, but the meridional wind itself is much slower at ~100 m/s. The phase speed difference between the two hemispheres can be attributed to the prevailing summer-to-winter circulation of background wind associated with the northern winter-like condition. One great advantage of numerical modeling is that it allows one to evaluate the different contributing factors to ion drift separately [*Richmond*, 1995], albeit only within the constraints of our knowledge of the underlining physical processes captured in the model. Figure 5b shows the vertical ion drift component associated with neutral winds. Because of the inclination angle between the magnetic field line and the vertical axis and the fact that ions move more freely along magnetic field lines, the equatorward wind surges push ions upward whereas poleward winds push ions downward. As a result, the UT-latitude distribution of the wind-driven vertical ion drift has the same propagation phase speed as the TADs. The electric field-driven vertical drift component is shown in Figure 5c. It should be noted that the TIMEGCM simulates self-consistently the dynamic and electrodynamic coupling processes in the thermosphere and ionosphere by taking into

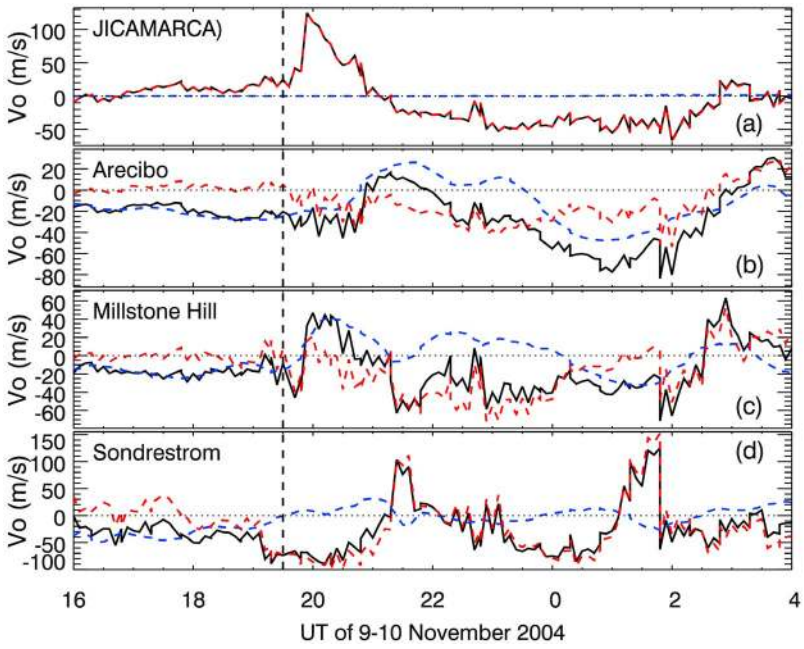


**Figure 6.** Modeled vertical ion drifts at the IS radar locations, with the blue dashed lines representing the wind-driven vertical drift component, the red dashed lines representing the electric field-driven component, and the black lines for the total vertical drift.

account the three-dimensional neutral wind distributions as well as electric conductivity owing to ion-neutral collisions. As shown in Figure 5c, the electric field-driven vertical ion drift at middle and low latitudes is upward from 19:30 UT to 21:00 UT, and then becomes downward until 02:30 UT on the next day. The total vertical ion drift is plotted in Figure 5d, which is the sum of the wind-driven vertical drift (Figure 5b) and electric field-driven vertical drift (Figure 5c). Since the wind-driven vertical ion drift is zero at the magnetic equator, the total vertical ion drift there is driven primarily by electric fields and therefore responds more promptly to the IEF. In the midlatitude region, however, the direction of the total vertical ion drift depends on the relative strength of these two different drivers. In this case and at this particular longitudinal sector, the wind-driven vertical ion drift exceeds the electric field-driven vertical drift. However, compared to the wind-driven vertical ion drift of ~30 m/s, the magnitude of the total vertical ion drift is increased to ~60 m/s at 40°N at the onset of the PPEF and later decreased to ~10 m/s below 30°N as indicated by the slanted dashed line.

[16] The relative contributions of disturbance meridional winds and electric fields are further elucidated in Figure 6, which shows the wind-driven (blue dashed lines) and electric field-driven (red dashed lines) vertical ion drift at the IS radar locations. At both Jicamarca (near the magnetic equator) and Sondrestrom (in the high-latitude auroral zone), vertical ion drift is primarily driven by electric fields. At Arecibo (at midlatitude), the large-scale variations in vertical ion drift are mainly controlled by meridional winds throughout the period from 16:00 UT on 9 November till about 03:00 UT on 10 November, whereas the small-scale variability appears to be modulations by electric fields. At Millstone Hill (in the sub-auroral zone), vertical drift is mainly driven by meridional winds prior to 19:30 UT, by electric fields from 19:30 to 20:00 UT, and mainly by winds again from 20:00 to ~21:15 UT. From 21:15 UT and onward, vertical ion drift at Millstone Hill is mostly driven by electric fields except for the interval of 00:15–01:45 UT on 10 November.

### 2.4. Electron Density Variations

[17] Figure 7 shows the modeled electron densities at the fixed 14:00 LT sector, and the white lines indicate the geomagnetic field lines along the corresponding LT meridian plane. Prior to the PPEF at 19:00 UT, the latitudinal distribution of electron density resembles a Λ-like structure owing to the rather small upward ion drift near the magnetic equator. The asymmetry about the magnetic equator is due in part to the asymmetric meridional wind, which is more poleward in the northern hemisphere than in the southern hemisphere because of the near-winter solstice condition. The peak density height at the magnetic equator is about 400 km at 19:00 UT. As the PPEF intensify from 19:30 UT to 20:00 UT, the electron density profile is kept nearly the same but the density peak height has risen to about 500 km. At 20:30 UT, the Λ–like profile has split into two density peaks on either side of the magnetic equator, forming the equatorial ionization anomaly (EIA) crests. Later at 21:00 and 21:30 UT, the two split density peaks continue to drop in height owing to the downward diffusion by gravity.

[18] Figure 8 shows global maps of total electron content (TEC) at selected UT times. The modeled TEC is calculated from the height-integrated electron density from ~35 km up to ~700 km (e.g., the altitude domain of the TIMECGM) though electron density is negligible below ~70 km. The black dashed curve in each panel indicates the magnetic equator. At 19:00 UT, the TEC map shows a single peak

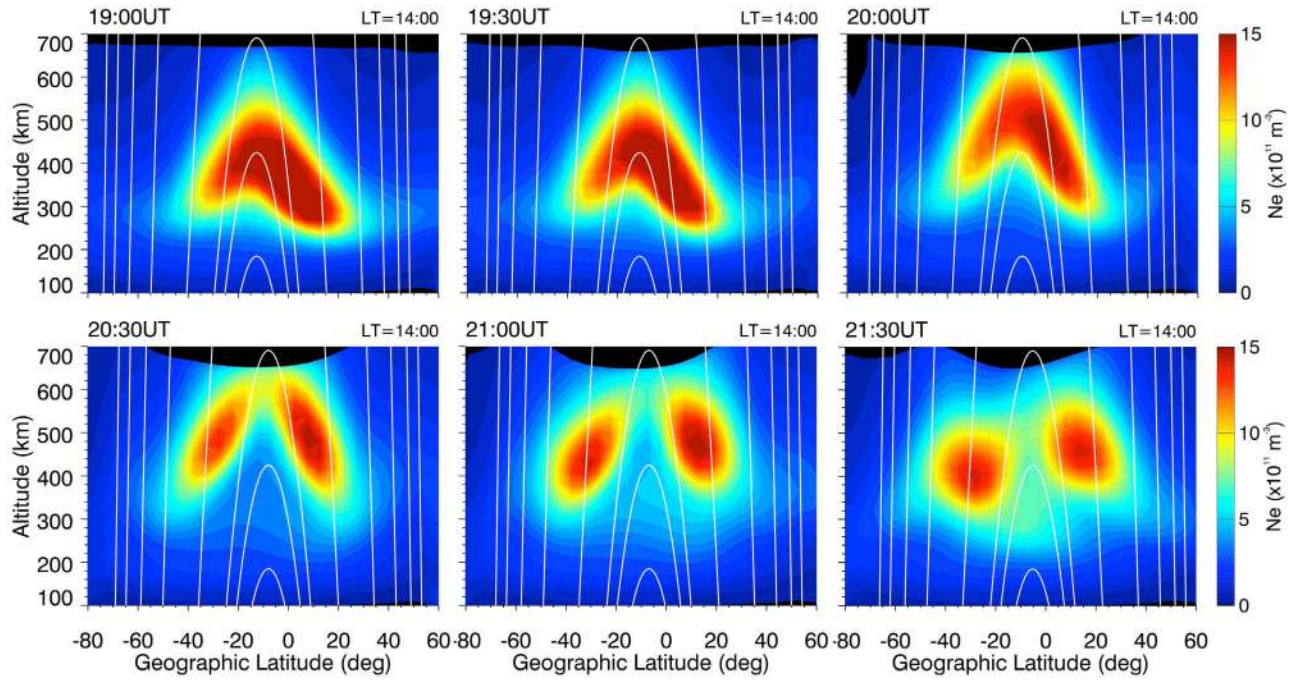


**Figure 7.** Altitude distributions of the modeled electron density at selected UT times. The white lines indicate the geomagnetic field lines.

near the magnetic equator. After the onset of the PPEF at 19:30 UT, the TEC morphology does not change immediately. About one hour later at 20:30 UT, there is a bifurcation of TEC around the magnetic equator. The equatorial TEC remains bifurcated at 21:00 UT and 21:30 UT, respectively. The bifurcation is the manifestation of the split of the *F* region electron density peaks illustrated in Figure 7.

[19] Changes in TEC can be caused by either dynamical or chemical process. To verify if chemical process plays a role in the observed TEC bifurcation, Figure 9 shows global

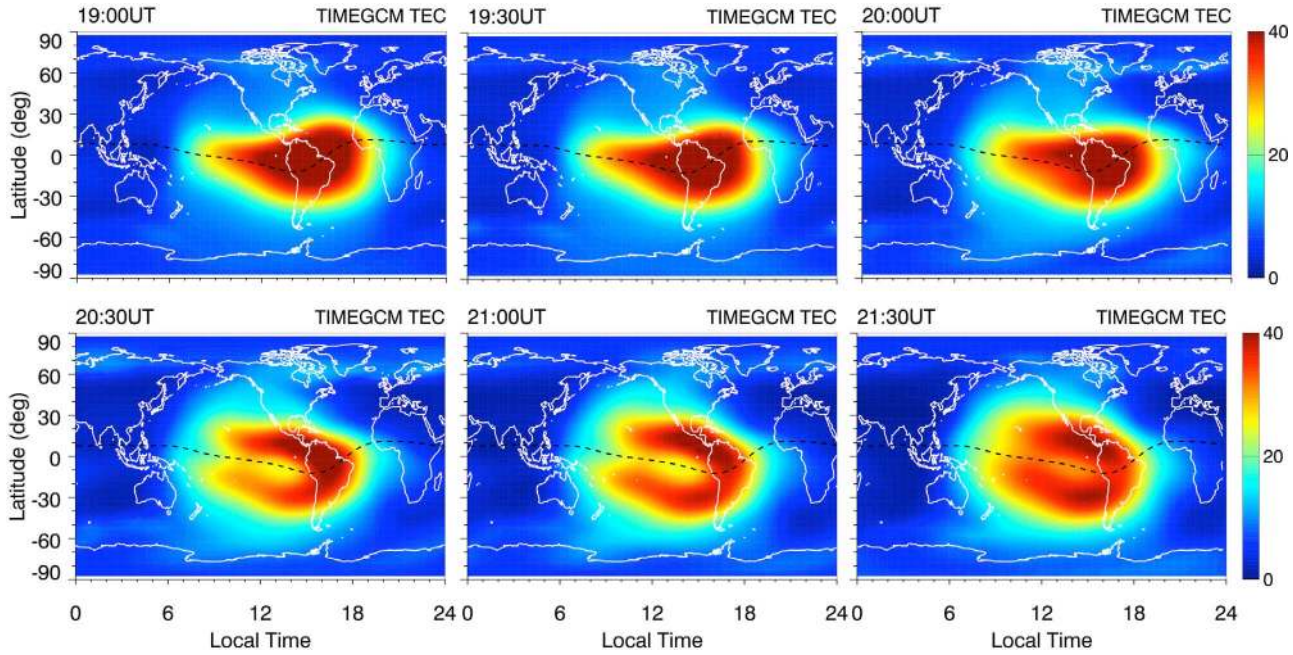


**Figure 8.** Global maps of the modeled TEC at selected UT times. Note that the color scale is from 0 to 40 TECU.

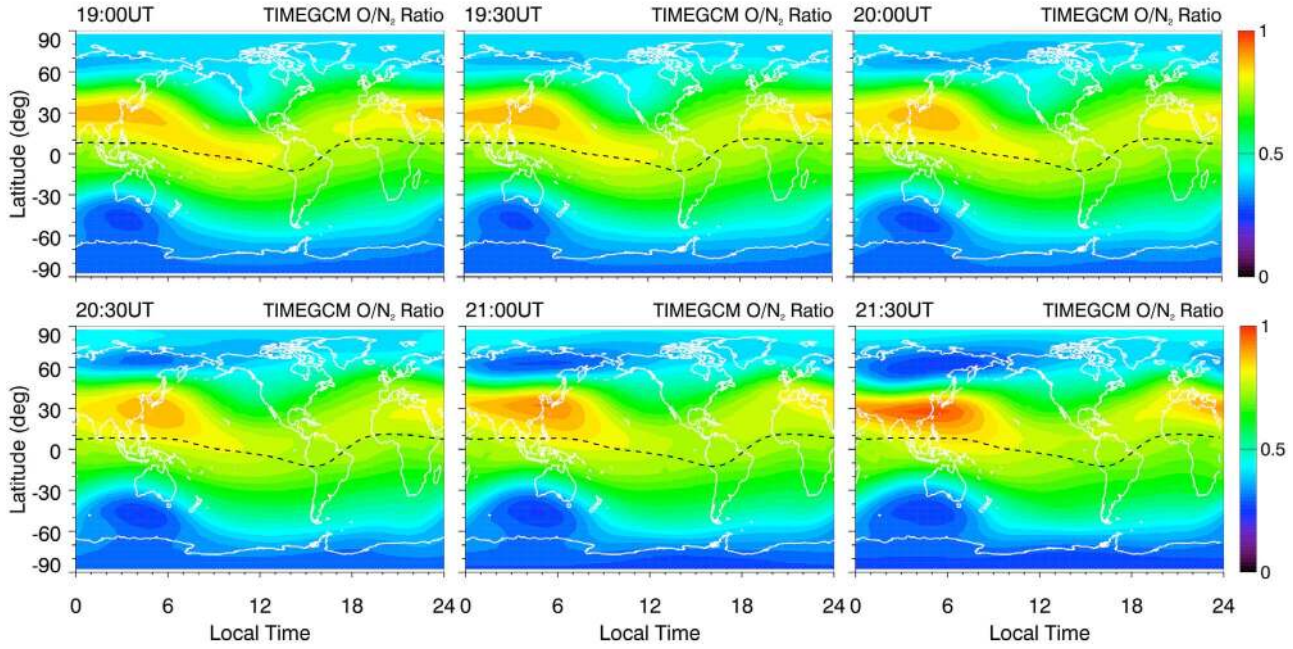


**Figure 9.** Global maps of the modeled O/N2 column density ratio at selected UT times.

distributions of the modeled $O/N_2$ column density ratio from the TIMEGCM, which is defined as the ratio of the O and $N_2$ column densities above the base height where the $N_2$ column density is of $10^{17}$ $cm^{-2}$, generally above ~130 km, in accordance with the GUVI measurements of thermospheric $O/N_2$ [*Strickland et al.*, 1995]. It is evident that the overall distribution of the $O/N_2$ ratio is nearly unaffected by the PPEF. This exercise allows us to rule out composition change as the main cause of the electron density variations in the F region.

## 3. Data and Model Comparison

[20] In order to validate the model performance in simulating the PPEF effects, we compare the model results with a

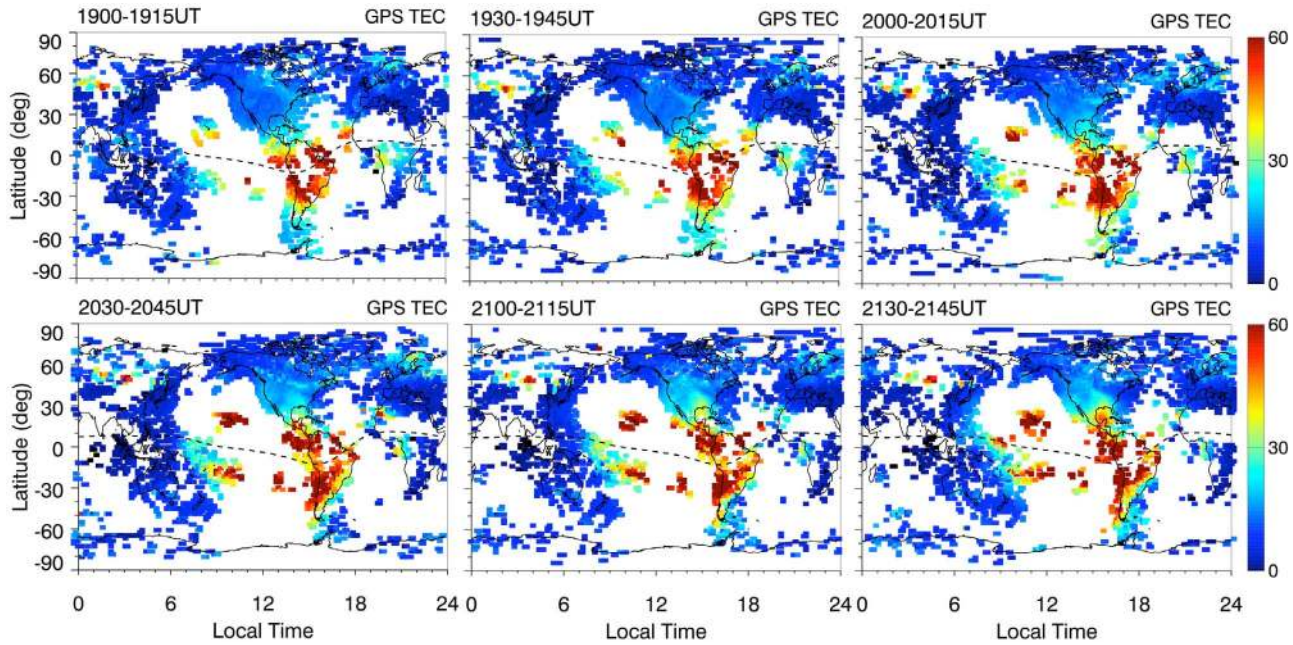


**Figure 10.** GPS TEC maps at selected UT. Note that the color scale is from 0 to 60 TECU, different from that used in Figure 8.

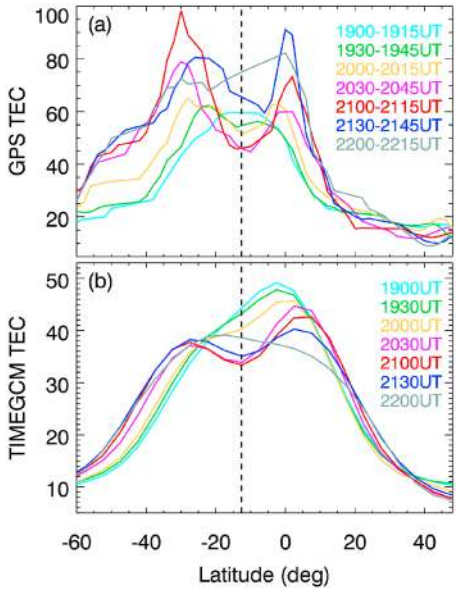


**Figure 11.** Latitudinal profiles of TEC from (a) the GPS measurements and (b) the TIMEGCM. The different colored lines correspond to the different UT times. The vertical dashed line in each panel indicates the geomagnetic equator.

number of key observations obtained during the event. Figure 10 shows the TEC maps derived from ground-based GPS receivers, and the data are obtained from the Madrigal database [*Rideout and Coster*, 2006]. Despite the data gaps over oceanic regions, the overall GPS-TEC morphology is similar to the simulated TEC maps shown in Figure 8. However, the bifurcation in the simulated TEC over the equatorial Pacific Ocean is not easily discernable in the GPS-TEC maps due to the large data gap there. For that reason, we examine more closely the TEC latitudinal profile along 75°W where the data coverage is relatively good across the magnetic equator. Figure 11a shows the GPS-TEC latitudinal profiles at selected UT times indicated by the different colored lines. Note that the GPS-TEC data are averaged over 5 degrees in latitude and longitude (from 72.5°W to 77.5°W) and 15 min in time. The vertical dashed line denotes the location of the magnetic equator at 75°W. At 19:00 UT, the GPS-TEC latitude profile is centered near the magnetic equator. From 19:30 UT to 2100 UT the GSP-TEC profile splits into two peaks, which gradually move away from the magnetic equator to about ±20° in magnetic latitude. At 21:30 UT, the TEC peaks retreat equatorward to about ±10° in magnetic latitude. By 22:00 UT, the twin-peak feature has diminished, forming a singe TEC peak near the geographic equator. Figure 11b shows the TIMEGCM-TEC latitudinal profile. The modeled TEC starts to evolve from a single peak profile into two split peaks at 20:00 UT, about 30 min later than the GPS observations. From 20:30 to 21:30 UT, a well-developed twin-peak structure is evident in the modeled TEC latitudinal profiles. At 22:00 UT, the modeled TEC returns to a single peak profile with its peak located near 20°S. At the magnetic equator, the TEC value gradually decreased from 19:00 UT to 21:00 UT when the IEF was positive, and then increased from 21:30 UT to 22:00 UT after the IEF became negative. Similar temporal variations are also evident in observations. The splitting TEC density peaks during the PPEF is consistent with the latitudinal TEC profiles obtained from the Boston College chain of GPS receivers in South America as shown in *Hei and Valladares* [2010] and *Retterer et al.* [2010]. These studies also successfully reproduced the splitting TEC phenomenon using 2D ionospheric models by applying prescribed neutral winds and vertical ion drift as input. In our simulation, however, all chemical, dynamical, and electrodynamical processes, including neutral winds and ion drifts, are computed self-consistently in the TIMEGCM.

[21] Significant quantitative differences exist between the data and our model results. For example, the GPS-TEC has a peak value about 100 TECU (1 TECU = $1 \times 10^{16}$ electrons/$m^2$) whereas the modeled TEC has a maximum value less than 50 TECU. The observed crest-to-trough ratio for the twin-peak structure is also about twice as large as the model results. Such differences can be attributed partly to the fact that the modeled TEC only accounts for electrons up to ~700 km (the upper boundary of the TIMEGCM) so the contribution by electrons at higher altitudes is not included. It has been estimated [*Lu et al.*, 1998] that the TEC above the model's upper boundary can be as large as the TEC calculated within the model altitude domain at low latitudes. Another contributing factor to the smaller crest-to-trough ratio in the model is that the upward plasma flux is capped by its upper boundary conditions (namely, the prescribed $O^+$ flux) that prevent more electrons at the magnetic equator from being lifted to higher altitude beyond the upper boundary of the model during the intense PPEF interval, which are subsequently displaced to higher latitudes due to downward diffusion along magnetic field lines; these electrons create the peak in both the electron density profile and

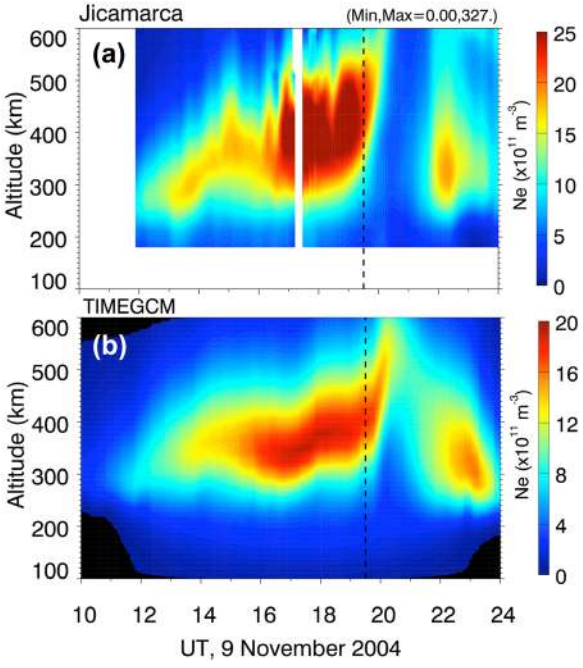


**Figure 12.** Comparison of electron density obtained from (a) the Jicamarca radar and (b) the TIMEGCM.

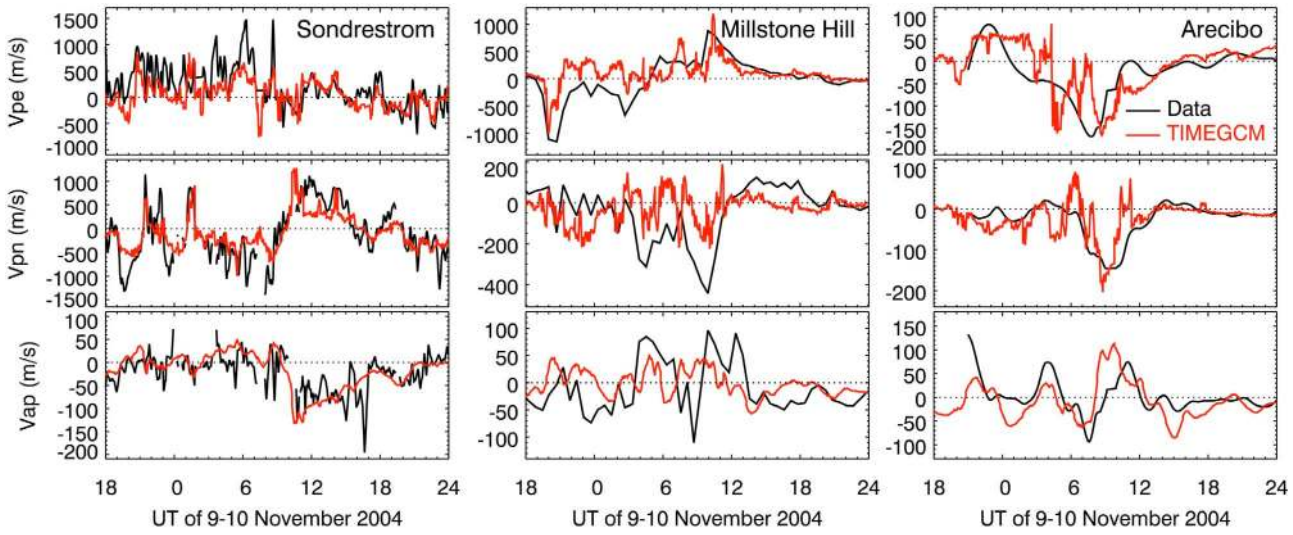


**Figure 13.** Comparison of the measured and modeled ion drifts over (left) Sondrestrom, (middle) Millstone Hill, and (right) Arecibo. Measurements are shown in black, and model results are in red.

in the latitudinal distribution of TEC before diffusing downward along magnetic field lines to higher latitudes.

[22] One potential effect of the $O^+$ flux upper boundary condition is illustrated in Figure 12, in which we show the UT-altitude distribution of electron density over Jicarmaca. The vertical dashed line marks the onset of the PPEF at 19:30 UT. The observed and modeled electron density distributions exhibit generally a similar morphology: a rapid rise in the electron peak height due to enhanced vertical drift associated with the PPEF at 19:30 UT, followed by a deep depletion of electron density from ~20:00 to 21:00 UT. The most noteworthy difference between the data and model is that the radar data indicate that the F-layer was lifted up to 1000 km, the upper range of the radar observations [*Kelley et al.*, 2010], whereas the modeled F-layer is kept below 600 km because the TIMEGCM does not allow plasmas to flow freely across its upper boundary.

[23] Full data sets from the North American IS radar chain (e.g., Jicamarca, Arecibo, Millstone Hill, and Sondrestrom) extending from the magnetic equator to the auroral zone are available from 21:00 UT on 9 November to 13 November. More detailed descriptions of radars' operational modes during that period can be found in *Kelley et al.* [2010] and in *Erickson et al.* [2010]. Comparison of vertical ion drift at Jicamarca has been shown in Figure 1e, which depicts a good data-model agreement on 9 November but less satisfactory comparison on 10 November. We now compare the measured and modeled ion drifts at Sondrestrom (left panel), Millstone Hill (middle panel), and Arecibo (right panel) in Figure 13, where *Vpe* is the eastward component of ion drift perpendicular to local magnetic field, *Vpn* is the northward ion drift component perpendicular to magnetic field, and *Vap* is the ion drift component anti-parallel to magnetic field. The radar measurements are shown in black and the model results are shown in red. Despite the complex nature of the PPEF on 9 November and multiple onsets of geomagnetic activity on 10 November, the modeled ion drift velocity shows a good qualitative agreement with the observations at all three radar locations. The comparison with the Sondrestrom radar measurements is particularly noteworthy. Since the Sondrestrom ion drift data were not part of the data input to AMIE in this case, the good agreement between the modeled and measured ion drift at Sondrestrom lends support for the notion that the AMIE outputs indeed represent rather well the true magnetospheric forcing for the event under study. However, large quantitative differences are evident between the data and the model results. For instance, many smaller-scale temporal structures shown in the model results at Millstone Hill and Arecibo are absent in the radar measurements. In this case, the Millstone Hill radar ion drift data had a temporal resolution of about 35 min. At Arecibo vector velocities were determined using dual-beam measurements and the regularization technique of *Sulzer et al.* [2005]. Vector measurements are acquired over the time for one full rotation of the dual beam radar (~15–20 min) but the regularization approach applies an effective low-pass filtering of the measurements. Also, the radar measurements have been averaged over the altitude range of 250–400 km, which further smoothes out small-scale structures.

[24] Finally, we compare the measured and modeled $O/N_2$ column density ratio. The TIMED satellite was in a sun-synchronous orbit, and the GUVI $O/N_2$ measurements were taken around 13:35 LT. We have sampled the model outputs along the satellite track in the same fashion as the GUVI observations were made. Figure 14 shows the GUVI measurements in the top panel, and the corresponding model results in the bottom panel. The vertical dotted lines indicate the PPEF interval from 19:30 UT to 21:30 UT. There is a good agreement between the GUVI and TIMEGCM in terms of the overall morphology, both showing large $O/N_2$ just north of the magnetic equator. However, there are also large quantitative differences between the GUVI measurements and the model results. For example, the GUVI data indicate larger $O/N_2$ ratio values in the northern and mid- and low-latitude region between 60°E and 160°E and a narrower band (and also more small-scale features) of $O/N_2$ between 180°W and 40°E compared to the model results. In the

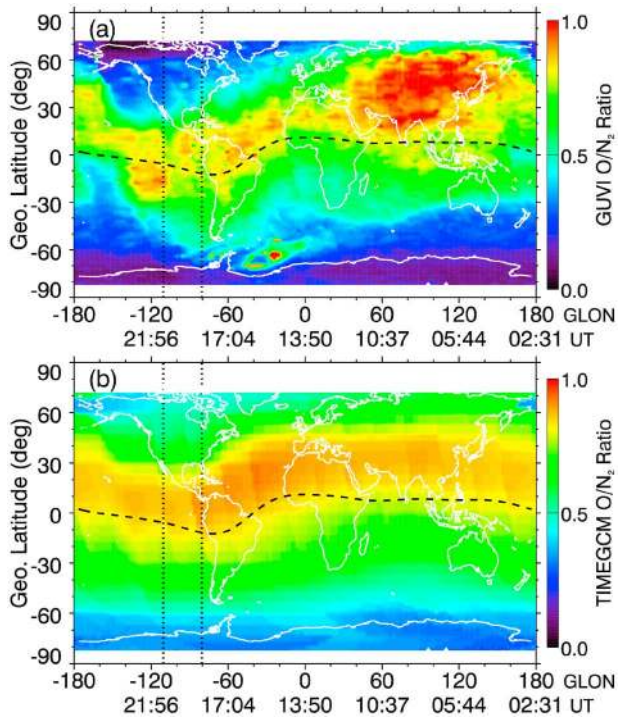


**Figure 14.** Comparison of the O/N2 column density ratio obtained from (top) GUVI and (bottom) the TIMEGCM. The black dashed curve in each panel indicates the magnetic equator. Note that the UT time goes from right to left in accordance with the GUVI scanning sequence. The vertical dotted lines indicate the PPEF interval from 19:30 UT to 21:30 UT.

southern hemisphere below 30°S, the modeled $O/N_2$ is slightly higher than the measured $O/N_2$. During the PPEF period marked by the dotted lines, however, neither GUVI nor the TIMEGCM show significant changes in $O/N_2$ that can be directly attributed to the bifurcation of equatorial TEC.

## 4. Summary and Discussion

[25] We have presented in this paper a comprehensive investigation of thermospheric and ionospheric response during a strong PPEF event on 9 November 2004. Using realistic time-dependent high-latitude forcing as represented by ionospheric convection and auroral precipitation patterns derived from AMIE, the TIMECGM is capable of reproducing many observed features associated with the PPEF, including the largest upward vertical ion drift ever recorded at Jicamarca. The detailed data-model intercomparison shows a generally good agreement in the overall morphology of electron density, ion drift velocities, global TEC, and the $O/N_2$ ratio. However, it is also evident that further improvements to the TIMEGCM are called for. More specifically, the model's upper boundary needs to be raised to higher altitude, and a more realistic $O^+$ flux specification needs to be implemented at its upper boundary. Ideally, the TIMECGM should be coupled with a realistic plasmasphere and the inner magnetosphere in order to eliminate the artificial upper boundary conditions. Such a coupled model will be a powerful tool to better understand the intricate dynamical and electrodynamical processes pertained to the PPEF events.

[26] Numerical experiments carried out in this study allow us to assess the relative contribution of electric fields and disturbance neutral winds to vertical ion drift. The model results confirm that the large vertical ion drift over Jicamarca on 9 November was indeed caused by high-latitude electric fields that had partly penetrated to lower latitudes. Though the coupled AMIE-TIMEGCM model is successful in reproducing the similar upward ion drift as measured by the Jicamarca radar, the model does not replicate electrodynamic interaction with the inner magnetosphere. Such interaction has been shown to have a significant influence on mid- and low-latitude dynamics [e.g., *Maruyama et al.*, 2005, 2007]. Theoretically, an electric field that penetrates to middle and low latitudes is expected to be damped out on time scales of 20 $\sim$ 30 min due to the formation of a shielding layer by charged particles at the inner edge of the plasma sheet, which cancels out convective electric field in the inner magnetosphere. Numerical simulations, however, have found that the shielding time can vary from 3 $\sim$ 5 min to a few hours depending on magnetospheric conditions as well as ionospheric conductivity [*Wolf*, 1970; *Wolf et al.*, 1982; *Senior and Blanc*, 1984; *Spiro et al.*, 1988; *Fejer et al.*, 1990]. Recent studies indicate that penetration electric field can persist for many hours after the IMF turns southward [*Huang et al.*, 2005, 2007; *Huang*, 2008; *Maruyama et al.*, 2007]. The fact that the coupled AMIE-TIMEGCM is able to reproduce the Jicamarca radar observations without the proper coupling to the inner magnetosphere may suggest that the magnetosphere did not have enough time to form an effective shielding layer during the 2-h interval of this strong PPEF. A possible cause for this ineffective shielding may lie in the fact that the PPEF coincided with the period when the magnetosheath region experienced a solar wind dynamic pressure that was about 5 times of its nominal value [*Lu et al.*, 2011]. High solar wind pressure and southward IMF cause the magnetotail to stretch, and thus prolong the development of the shielding layer in the inner magnetosphere [*Sazykin et al.*, 2005; *Maruyama et al.*, 2007]. Furthermore, high solar wind speed and negative IMF $B_z$ are known to cause particle energization and increase the plasma sheet temperature [e.g., *Tsyganenko and Mukai*, 2003]. As shown by numerical simulations, the hotter the plasma sheet, the weaker the shielding is [*Spiro et al.*, 1988; *Garner et al.*, 2004].

[27] In the midlatitude region, vertical ion drift is subject to both electric fields and disturbance meridional winds. The direction of vertical ion drift depends on the relative strength of these two different drivers. In this case, the magnitude of the wind-driven vertical ion drift exceeds the electric field-driven vertical drift at midlatitudes in both hemispheres. However, the wind-driven vertical drift diminishes toward the magnetic equator where the electric field-driven vertical drift becomes dominant.

[28] As shown in statistical models [e.g., *Fejer and Scherliess*, 1995, 1997], equatorial vertical ion drift associated with the penetration electric field is highly variable, and its strength and direction depends on local time. Generally speaking, when the IEF is positive (or the IMF is southward), vertical ion drift is upward on the dayside and downward on the nightside. The coupled AMIE-TIMEGCM

simulation reaffirms this general conclusion with regard to the local-time variations of the PPEF. The model also shows that the local-time variations of vertical ion drift are more complicated than a simple sinusoidal function and the boundary between the upward and downward vertical drift may vary with UT.

[29] Poleward expansion of low-latitude TEC to as far as $30^\circ \sim 40^\circ$ away from the magnetic equator has been observed during major geomagnetic storms, and is attributed to the dayside "super-fountain" effect [*Tsurutani, et al.*, 2004; *Mannucci et al.*, 2005; *Astafyeva*, 2009]. The coupled AMIE-TIMEGCM allows us to examine this effect explicitly during this well-observed PPEF event. Our simulation is able to capture the evolution of the UT-latitude profiles of electron density associated with the PPEF, including the initial uplift of the F-layer, the split of density peaks, and the subsequent downward and poleward motion. Consequently, the dayside low-latitude TEC gradually splits around the magnetic equator to about $\pm 20^\circ$ magnetic latitude. As noted by *Lin et al.* [2005] and *Retterer et al.* [2010], the TEC crests that are primarily driven by eastward electric field can be further enhanced by equatorward meridional winds that push plasmas upward along magnetic field lines where recombination rate becomes smaller. In this case, strong equatorward wind surges are produced by high-latitude Joule heating enhancement due to the same IEF responsible for the PPEF, and thus contribute positively to the TEC bifurcation. However, due to the upper boundary conditions imposed on the TIMEGCM, the overall "super-fountain" effect is likely to be underestimated by the model.

[30] **Acknowledgments.** The MIT Haystack Observatory is supported by National Science Foundation (NSF) Co-operative Agreement ATM-0733510 with the Massachusetts Institute of Technology, and the Sondrestrom ISR is operated by SRI International under NSF cooperative agreement ATM-0836152. The Arecibo Observatory is operated through a cooperative agreement with the NSF. Work at HAO/NCAR was supported in part by NASA's Heliophysics Guest Investigators Program under grant NNH09AK621. NCAR is sponsored by the NSF.

[31] Robert Lysak thanks the reviewers for their assistance in evaluating this paper.

## References

Anderson, D. N. (1973), A theoretical study of the ionospheric F region equatorial anomaly: I. Theory, *Planet. Space Sci.*, *21*, 409–419, doi:10.1016/0032-0633(73)90040-8.

Astafyeva, E. (2009), Effects of strong IMF $B_z$ southward events on the equatorial and mid-latitude ionosphere, *Ann. Geophys.*, *27*, 1175–1187, doi:10.5194/angeo-27-1175-2009.

Basu, S., et al. (2001), Ionospheric effects of major magnetic storms during the International Space Weather Period of September and October 1999: GPS observations, VHF/UHF scintillations, and in situ density structures at middle and equatorial latitudes, *J. Geophys. Res.*, *106*(A12), 30,389–30,413, doi:10.1029/2001JA001116.

Erickson, P. J., L. P. Goncharenko, M. J. Nicolls, M. Ruohoniemi, and M. C. Kelley (2010), Dynamics of North American sector ionospheric and thermospheric response during the November 2004 superstorm, *J. Atmos. Sol. Terr. Phys.*, *72*, 292–301, doi:10.1016/j.jastp.2009.04.001.

Fejer, B. G., and L. Scherliess (1995), Time dependent response of equatorial ionospheric electric fields to magnetospheric disturbances, *Geophys. Res. Lett.*, *22*(7), 851–854, doi:10.1029/95GL00390.

Fejer, B. G., and L. Scherliess (1997), Empirical models of storm time equatorial zonal electric fields, *J. Geophys. Res.*, *102*(A11), 24,047–24,056, doi:10.1029/97JA02164.

Fejer, B. G., R. W. Spiro, R. A. Wolf, and J. C. Foster (1990), Latitudinal variation of perturbation electric fields during magnetically disturbed periods: 1986 Sundial observations and model results, *Ann. Geophys.*, *8*, 441–454.

Fejer, B. G., L. Scherliess, and E. R. de Paula (1999), Effects of the vertical plasma drift velocity on the generation and evolution of equatorial spread *F*, *J. Geophys. Res.*, *104*(A9), 19,859–19,869, doi:10.1029/1999JA900271.

Fejer, B. G., J. W. Jensen, T. Kikuchi, M. A. Abdu, and J. L. Chau (2007), Equatorial ionospheric electric fields during the November 2004 magnetic storm, *J. Geophys. Res.*, *112*, A10304, doi:10.1029/2007JA012376.

Fesen, C. G., G. Crowley, R. G. Roble, A. D. Richmond, and B. G. Fejer (2000), Simulation of the pre-reversal enhancement in the low latitude vertical ion drifts, *Geophys. Res. Lett.*, *27*(13), 1851–1854, doi:10.1029/2000GL000061.

Gallagher, D. L., P. D. Craven, and R. H. Comfort (2000), Global core plasma model, *J. Geophys. Res.*, *105*(A8), 18,819–18,833, doi:10.1029/1999JA000241.

Garner, T. W., R. A. Wolf, R. W. Spiro, W. J. Burke, B. G. Fejer, S. Sazykin, J. L. Roeder, and M. R. Hairston (2004), Magnetospheric electric fields and plasma sheet injection to low L-shells during the 4–5 June 1991 magnetic storm: Comparison between the Rice Convection Model and observations, *J. Geophys. Res.*, *109*, A02214, doi:10.1029/2003JA010208.

Gonzalez, W. D., J. A. Joselyn, Y. Kamide, H. W. Kroehl, G. Rostoker, B. T. Tsurutani, and V. M. Vasyliunas (1994), What is a geomagnetic storm?, *J. Geophys. Res.*, *99*(A4), 5771–5792, doi:10.1029/93JA02867.

Grigorenko, E. I., V. N. Lysenko, S. A. Pazyura, V. I. Taran, and L. F. Chernogor (2007), Ionospheric disturbances during the severe magnetic storm of November 7–10, 2004, *Geomagn. Aeron.*, Engl. Transl., *47*(6), 720–738, doi:10.1134/S0016793207060059.

Hagan, M. E., and J. M. Forbes (2002), Migrating and nonmigrating diurnal tides in the middle and upper atmosphere excited by tropospheric latent heat release, *J. Geophys. Res.*, *107*(D24), 4754, doi:10.1029/2001JD001236.

Hagan, M. E., and J. M. Forbes (2003), Migrating and nonmigrating semidiurnal tides in the upper atmosphere excited by tropospheric latent heat release, *J. Geophys. Res.*, *108*(A2), 1062, doi:10.1029/2002JA009466.

Hanson, W. B., and R. J. Moffet (1966), Ionization transport effects in the equatorial *F* region ionosphere, *J. Geophys. Res.*, *71*(23), 5559, doi:10.1029/JZ071i023p05559.

Hei, M. A., and C. E. Valladares (2010), The November 2004 superstorm: Comparison of low-latitude TEC observations with LLIONS model results, *J. Atmos. Sol. Terr. Phys.*, *72*, 334–343, doi:10.1016/j.jastp.2009.03.025.

Huang, C.-S. (2008), Continuous penetration of the interplanetary electric field to the equatorial ionosphere over eight hours during intense geomagnetic storms, *J. Geophys. Res.*, *113*, A11305, doi:10.1029/2008JA013588.

Huang, C.-S., J. C. Foster, and M. C. Kelley (2005), Long-duration penetration of the interplanetary electric field to the low-latitude ionosphere during the main phase of magnetic storms, *J. Geophys. Res.*, *110*, A11309, doi:10.1029/2005JA011202.

Huang, C.-S., S. Sazykin, J. L. Chau, N. Maruyama, and M. C. Kelley (2007), Penetration electric fields: Efficiency and characteristic time scale, *J. Atmos. Sol. Terr. Phys.*, *69*, 1135–1146, doi:10.1016/j.jastp.2006.08.016.

Kelley, M. C., and J. Retterer (2008), First successful prediction of a convective equatorial ionospheric storm using solar wind parameters, *Space Weather*, *6*, S08003, doi:10.1029/2007SW000381.

Kelley, M. C., R. R. Ilma, M. Nicolls, P. Erickson, L. Goncharenko, J. L. Chau, N. Aponte, and J. U. Kozyra (2010), Spectacular low- and mid-latitude electrical fields and neutral winds during a superstorm, *J. Atmos. Sol. Terr. Phys.*, *72*, 285–291, doi:10.1016/j.jastp.2008.12.006.

King, J. W. (1968), Airglow observations and the decay of the ionospheric equatorial anomaly, *J. Atmos. Terr. Phys.*, *30*, 391–402, doi:10.1016/0021-9169(68)90110-4.

Lin, C. H., A. D. Richmond, R. A. Heelis, G. J. Bailey, G. Lu, J. Y. Liu, H. C. Yeh, and S.-Y. Su (2005), Theoretical study of the low- and midlatitude ionospheric electron density enhancement during the October 2003 superstorm: Relative importance of the neutral wind and the electric field, *J. Geophys. Res.*, *110*, A12312, doi:10.1029/2005JA011304.

Lu, G., X. Pi, A. D. Richmond, and R. G. Roble (1998), Variations of total electron content during geomagnetic disturbances: A model/observation comparison, *Geophys. Res. Lett.*, *25*(3), 253–256, doi:10.1029/97GL03778.

Lu, G., A. D. Richmond, R. G. Roble, and B. A. Emery (2001), Coexistence of ionospheric positive and negative storm phases under northern winter conditions: A case study, *J. Geophys. Res.*, *106*(A11), 24,493–24,504, doi:10.1029/2001JA000003.

Lu, G., et al. (2011), Reversed two-cell convection in the Northern and Southern hemispheres during northward interplanetary magnetic field, *J. Geophys. Res.*, *116*, A12237, doi:10.1029/2011JA017043.

Mannucci, A. J., B. T. Tsurutani, B. A. Iijima, A. Komjathy, A. Saito, W. D. Gonzalez, F. L. Guarnieri, J. U. Kozyra, and R. Skoug (2005), Dayside global ionospheric response to the major interplanetary events of October 29–30, 2003 "Halloween Storms", *Geophys. Res. Lett.*, *32*, L12S02, doi:10.1029/2004GL021467.

Mannucci, A. J., B. T. Tsurutani, M. C. Kelley, B. A. Iijima, and A. Komjathy (2009), Local time dependence of the prompt ionospheric response for the 7, 9, and 10 November 2004 superstorms, *J. Geophys. Res.*, *114*, A10308, doi:10.1029/2009JA014043.

Maruyama, N., A. D. Richmond, T. J. Fuller-Rowell, M. V. Codrescu, S. Sazykin, F. R. Toffoletto, R. W. Spiro, and G. H. Millward (2005), Interaction between direct penetration and disturbance dynamo electric fields in the storm-time equatorial ionosphere, *Geophys. Res. Lett.*, *32*, L17105, doi:10.1029/2005GL023763.

Maruyama, N., et al. (2007), Modeling storm-time electrodynamics of the low-latitude ionosphere–thermosphere system: Can long lasting disturbance electric fields be accounted for?, *J. Atmos. Sol. Terr. Phys.*, *69*, 1182–1199, doi:10.1016/j.jastp.2006.08.020.

Pierrard, V., and K. Stegen (2008), A three-dimensional dynamic kinetic model of the plasmasphere, *J. Geophys. Res.*, *113*, A10209, doi:10.1029/2008JA013060.

Retterer, J. M., and M. C. Kelley (2010), Solar wind drivers for low-latitude ionosphere models during geomagnetic storms, *J. Atmos. Sol. Terr. Phys.*, *72*, 344–349, doi:10.1016/j.jastp.2009.07.003.

Retterer, J. M., R. Ilma, M. C. Kelley, J. L. Chau, C. E. Valladares, L. C. Gentile, and K. Groves (2010), Modeling the low-latitude ionospheric electron density and plasma turbulence in the November 2004 storm period, *J. Atmos. Sol. Terr. Phys.*, *72*, 350–357, doi:10.1016/j.jastp.2009.07.012.

Richmond, A. D. (1995), Ionospheric electrodynamics, in *Handbook of Atmospheric Electrodynamics*, *2*, edited by H. Volland, pp. 249–290, CRC Press, Boca Raton, Fla.

Richmond, A. D., and Y. Kamide (1988), Mapping electrodynamic features of the high-latitude ionosphere from localized observations: Technique, *J. Geophys. Res.*, *93*(A6), 5741–5759, doi:10.1029/JA093iA06p05741.

Rideout, W., and A. J. Coster (2006), Automated GPS processing for global total electron content data, *GPS Solut.*, *10*, 219, doi:10.1007/s10291-006-0029-5.

Roble, R. G., and E. C. Ridley (1994), A thermosphere-ionosphere-mesosphere- electrodynamics general circulation model (time-GCM): Equinox solar cycle minimum simulations (30–500 km), *Geophys. Res. Lett.*, *21*(6), 417–420, doi:10.1029/93GL03391.

Sahai, Y., et al. (2009a), Effects observed in the Latin American sector ionospheric *F* region during the intense geomagnetic disturbances in the early part of November 2004, *J. Geophys. Res.*, *114*, A00A19, doi:10.1029/2007JA013007.

Sahai, Y., et al. (2009b), Effects observed in the ionospheric *F* region in the east Asian sector during the intense geomagnetic disturbances in the early part of November 2004, *J. Geophys. Res.*, *114*, A00A18, doi:10.1029/2008JA013053.

Sazykin, S., R. W. Spiro, R. A. Wolf, F. R. Toffoletto, N. Tsyganenko, J. Goldstein, and M. R. Hairston (2005), Modeling inner magnetospheric electric fields: Latest self-consistent results, in *The Inner Magnetosphere: Physics and Modeling*, *Geophys. Monogr. Ser*, vol. 155, edited by T. I. Pulkkinen, N. A. Tsyganenko, and R. H. Friedel, pp. 263–269, AGU, Washington, D. C.

Senior, C., and M. Blanc (1984), On the control of magnetospheric convection by the spatial distribution of ionospheric conductivities, *J. Geophys. Res.*, *89*(A1), 261–284, doi:10.1029/JA089iA01p00261.

Spiro, R. W., R. A. Wolf, and B. G. Fejer (1988), Penetration of high-latitude-electric-field effects to low latitudes during Sundial 1984, *Ann. Geophys.*, *6*, 39–49.

Strickland, D. J., J. S. Evans, and L. J. Paxton (1995), Satellite remote sensing of thermospheric $O/N_2$ and solar EUV, 1. Theory, *J. Geophys. Res.*, *100*(A7), 12,217–12,226, doi:10.1029/95JA00574.

Sulzer, M. P., N. Aponte, and S. A. González (2005), Application of linear regularization methods to Arecibo vector velocities, *J. Geophys. Res.*, *110*, A10305, doi:10.1029/2005JA011042.

Tsurutani, B., et al. (2004), Global dayside ionospheric uplift and enhancement associated with interplanetary electric fields, *J. Geophys. Res.*, *109*, A08302, doi:10.1029/2003JA010342.

Tsyganenko, N. A., and T. Mukai (2003), Tail plasma sheet models derived from Geotail particle data, *J. Geophys. Res.*, *108*(A3), 1136, doi:10.1029/2002JA009707.

Wolf, R. A. (1970), Effects of ionospheric conductivity on convective flow of plasma in the magnetosphere, *J. Geophys. Res.*, *75*(25), 4677–4698, doi:10.1029/JA075i025p04677.

Wolf, R. A., M. Harel, R. W. Spiro, G.-H. Voigt, P. H. Reiff, and C.-K. Chen (1982), Computer simulation of inner magnetospheric dynamics for the magnetic storm of July 29, 1977, *J. Geophys. Res.*, *87*(A8), 5949–5962, doi:10.1029/JA087iA08p05949.

Woodman, R. F. (1970), Vertical drift velocities and east-west electric fields at the magnetic equator, *J. Geophys. Res.*, *75*(31), 6249–6259, doi:10.1029/JA075i031p06249.